

# Gapping the spin-nodal planes of an anisotropic $p$ -wave magnet to induce a large anomalous Hall effect

Rinsuke Yamada<sup>1,¶,\*</sup>, Max T. Birch<sup>2,¶</sup>, Priya R. Baral<sup>1,¶</sup>, Shun Okumura<sup>1</sup>, Ryota Nakano<sup>1</sup>, Shang Gao<sup>2,§</sup>, Yuki Ishihara<sup>1</sup>, Kamil K. Kolincio<sup>2,3</sup>, Ilya Belopolski<sup>2</sup>, Hajime Sagayama<sup>4</sup>, Hironori Nakao<sup>4</sup>, Kazuki Ohishi<sup>5</sup>, Taro Nakajima<sup>6</sup>, Yoshinori Tokura<sup>1,2,7</sup>, Taka-hisa Arima<sup>2,8</sup>, Yukitoshi Motome<sup>1</sup>, Moritz M. Hirschmann<sup>2</sup>, and Max Hirschberger<sup>1,2,†</sup>

<sup>1</sup>*Department of Applied Physics and Quantum-Phase Electronics Center,*

*The University of Tokyo, Bunkyo, Tokyo 113-8656, Japan*

<sup>2</sup>*RIKEN Center for Emergent Matter Science (CEMS), Wako, Saitama 351-0198, Japan*

<sup>3</sup>*Faculty of Applied Physics and Mathematics, Gdańsk University of Technology, Narutowicza 11/12, 80-233 Gdańsk, Poland*

<sup>4</sup>*Institute of Materials Structure Science, High Energy Accelerator Research Organization, Tsukuba, Ibaraki 305-0801, Japan*

<sup>5</sup>*Neutron Science and Technology Center, Comprehensive Research*

*Organization for Science and Society (CROSS), Tokai, Ibaraki 319-1106, Japan*

<sup>6</sup>*The Institute for Solid State Physics, University of Tokyo, Kashiwa, Chiba 277-8561, Japan*

<sup>7</sup>*Tokyo College, University of Tokyo, Bunkyo, Tokyo 113-8656, Japan*

<sup>8</sup>*Department of Advanced Materials Science, The University of Tokyo, Kashiwa, Chiba 277-8561, Japan*

<sup>§</sup>*Current address: Department of Physics, University of Science and Technology of China, Hefei 230026, China and*

<sup>¶</sup>*Equal contribution*

Antiferromagnets with spin splitting in the electronic structure are desired for novel spintronic phenomena in materials with nearly zero net magnetization [1–6]. One of the simplest spin-split antiferromagnetic states, the  $p$ -wave magnet, is proposed as a result of collective instability of electron gases [7–11]. Following a more recent theoretical proposal without strong electron correlations [12, 13], we here report a material with the symmetry constraints for  $p$ -wave magnetism of conduction electrons in momentum space, based on a texture of magnetic moments in direct space. Our resonant X-ray scattering reveals coplanar, lattice-locked antiferromagnetism that satisfies the required conditions for a  $p$ -wave magnet: it breaks space inversion, but preserves time-reversal ( $\mathcal{T}$ ) symmetry up to a positional shift in direct space. Consistent with theoretical predictions, the electric conductivity is characteristically anisotropic in this  $p$ -wave magnet [12–14]. In conducting magnets, the coupling of magnetic spins and freely moving electrons favors small distortions of the  $p$ -wave state, slightly breaking the  $\mathcal{T}$  symmetry and inducing a tiny net magnetization [15]. In our material, this gentle symmetry breaking induces an anomalous Hall effect (AHE) with a giant anomalous Hall conductivity for a bulk antiferromagnet,  $\sigma_{xy} > 600$  S/cm (Hall angle  $> 3\%$ ). The  $p$ -wave magnet has characteristic spin-nodal planes, and such a giant AHE can be attributed to hybridization of electron bands around these nodal regions due to  $\mathcal{T}$  breaking.

The spin splitting of electronic band states in momentum space is deeply intertwined with the texture of magnetic moments in direct space – and its symmetries [1–5, 12]. This is exemplified by the contrasting electronic structures of a  $p$ -wave (antiferro-)magnet and a ferromagnet (Fig. 1a, b). The ferromagnetic state with its uniform net magnetization in direct space results in different energies for spin-up and spin-down ( $\uparrow, \downarrow$ ) electron bands in momentum space. The resulting net spin polarization of band states is depicted by a circle and blue bars in Fig. 1b, which – in the language of spherical harmonics – can be described as an isotropic  $s$ -wave. In contrast, the  $p$ -wave magnet can be illustrated as an anisotropic spin-split Fermi surface with a unique quantization axis for  $\uparrow, \downarrow$ . Figure 1a depicts this spin splitting in momentum space, characterized by a spin polarization vector  $\boldsymbol{\alpha}$ , and an example of a corresponding magnetic texture in direct space. To allow for the anisotropic spin splitting of the  $p$ -wave magnet, it is necessary to break space inversion symmetry. To guarantee the unique spin quantization axis for  $\uparrow, \downarrow$  bands and zero net magnetization, we further require two symmetries [4, 5, 13]: first, a  $180^\circ$  rotation around an axis perpendicular to all spins,  $C_{2\perp}$ , paired with a translation by half a magnetic period in direct space,  $\boldsymbol{t}_{1/2}$ . Second, a time reversal (TR) operation  $\mathcal{T}$  paired with  $\boldsymbol{t}_{1/2}$ .

In the field of strong correlations and many-body physics, the realization of a  $p$ -wave magnet with unique spin quantization axis has long been sought as an electronic analogue to the  $A$ -phase of superfluid helium-3 [7, 8, 11]. More recently,  $p$ -wave magnets without strong correlations have been proposed based on symmetry considerations, as indicated above, and various  $p$ -wave candidate materials were identified [12, 13]. However, the expected anisotropic electronic transport response [12, 14] of a  $p$ -wave magnet has not been reported so far, and the effect of relativistic

\*Electronic address: ryamada@ap.t.u-tokyo.ac.jp

†Electronic address: hirschberger@ap.t.u-tokyo.ac.jp

spin-orbit coupling (SOC) on the  $p$ -wave electronic structure has not been discussed in a real-world setting.

We use a low-energy, single orbital model of the electronic structure to discuss the functional responses of spin-split  $p$ -wave magnets, which are tied to their requisite symmetries (Fig. 1c). The spin quantization of the electronic bands is along the  $k_x$  direction and the spin polarization of band states is represented by the colour code, where  $\uparrow$  and  $\downarrow$  are shown in red and blue, respectively. There is a line of states where  $\uparrow$  and  $\downarrow$  bands touch, indicated by the black parabola: this is the spin-nodal plane. In this scenario, anisotropic charge flow is naturally expected due to the difference in electronic structure along the  $k_x$  and  $k_y$  axes [6, 12–14, 16, 17]. Figure 1e shows the model’s momentum-resolved expectation value for the spin component  $S_x$  at the chemical potential, as well as the spin-nodal plane. Breaking of  $\mathcal{T}$  symmetry for the  $p$ -wave state can also be considered in this model: adding a small net magnetization  $m_z$  along the  $k_z$  direction as well as spin-orbit coupling, we open a hybridization gap on the spin-nodal plane, illustrated in Fig. 1d. This band mixing generates an emergent magnetic field in  $\mathbf{k}$ -space, termed Berry curvature (Fig. 1f), which drives an anomalous Hall effect (AHE) detected as a voltage along the  $y$ -axis when the current is along the  $x$ -axis of the distorted  $p$ -wave magnet. We stress that – in contrast to other spin-split antiferromagnets of recent interest, such as  $d$ - or  $g$ -wave *altersmagnets* [4, 5] – the  $p$ -wave spin splitting does not, perforce, violate  $\mathcal{T}$ . Instead, the AHE emerges only in presence of a  $\mathcal{T}$ -breaking  $m_z \neq 0$ .

### Search for a candidate $p$ -wave magnet

The symmetry requirements for the  $p$ -wave state are satisfied by a certain type of coplanar spin helix in direct space, which expands the crystallographic unit cell  $N$ -fold [12, 13]. Here,  $N$  must be an even number. This state naturally breaks the space inversion, or parity, symmetry. We select the intermetallic  $\text{Gd}_3\text{Ru}_4\text{Al}_{12}$  as a material platform with helical magnetic order [18, 19], where spin-spin interactions are mediated by conduction electrons [20–22] (Fig. 2a). Systematically changing the band filling by replacing Rh for Ru in  $\text{Gd}_3(\text{Ru}_{1-x}\text{Rh}_x)_4\text{Al}_{12}$  (Methods), we search for a lattice-matched, commensurate spin helix, where both  $[C_{2\perp} \parallel \mathbf{t}_{1/2}]$  and  $[\mathcal{T} \parallel \mathbf{t}_{1/2}]$  symmetries can be satisfied. Around  $x \approx 0.05$ , a novel magnetic phase emerges with signatures of  $p$ -wave magnetism, as discussed in the following (Fig. 2b).

To address the possibility for lattice-commensurate locking, we use resonant elastic X-ray scattering (REXS) measurements (Fig. 2c). The incident photon energy of a synchrotron light source is tuned to match the  $\text{Gd-}L_2$  absorption edge, where magnetic scattering is enhanced (Methods). We use REXS to track the magnetic reflections in  $\mathbf{k}$ -space while varying  $x$ , observing the propagation vector  $\mathbf{k}_{\text{mag}}$  of the magnetic wave and its direction relative to the crystal axes. The position of  $\mathbf{k}_{\text{mag}}$  in the Brillouin zone is illustrated in the inset of Fig. 2b. Here, blue, red, and black symbols indicate  $\mathbf{k}_{\text{mag}}$  for  $x = 0, 0.05$ , and  $0.20$ , respectively. In a limited window of composition around  $x \approx 0.05$ , the magnetic satellites are labelled by the Miller indices  $(1/6, 1/6, 0)$ . Thus, the magnetic period is well matched to the crystal lattice and expands the size of the unit cell six-fold ( $N = 6$ ). The reconstructed unit cell is shown by the orange box in Fig. 2d. Supporting neutron scattering experiments demonstrate the absence of other magnetic reflections. A detailed characterization of all single crystals grown for this study is shown in Supplementary Information.

### Coplanar antiferromagnetism from resonant X-ray scattering

One of the requirements for  $p$ -wave magnetism is the  $C_{2\perp}$  spin rotation symmetry around a common axis, paired with a half-unit cell translation  $\mathbf{t}_{1/2}$ . This means that all spins in direct space should be coplanar, that is, aligned in a common plane. To reveal the direction of magnetic spins, we perform X-ray polarization analysis in the experimental geometry of Fig. 2c, where the incoming beam  $\mathbf{k}_i$  and the outgoing beam  $\mathbf{k}_f$  span the scattering plane (grey shaded, semi-circular plane). The polarization of incident X-rays is in the scattering plane ( $\pi$ -polarized), while we detect both horizontal ( $\pi'$ ) and vertical ( $\sigma'$ ) components of the scattered beam. The corresponding intensities are  $I_{\pi-\pi'}$  and  $I_{\pi-\sigma'}$ , respectively. Briefly summarizing the discussion in Methods, the  $\pi - \pi'$  channel probes the magnetic moment perpendicular to the scattering plane,  $I_{\pi-\pi'} \propto m_z^2$ , whereas the  $\pi - \sigma'$  channel is  $I_{\pi-\sigma'} \propto (\mathbf{k}_i \cdot \mathbf{m}_{\text{ip}})^2$  [23]. Here,  $\mathbf{m}_{\text{ip}}$  is the projection of the magnetic moment onto the scattering plane.

We focus on three magnetic reflections in a single Brillouin zone, illustrated in Fig. 2e. The experiment in Fig. 2f-h evidences  $I_{\pi-\pi'}$  intensity for all three, demonstrating that  $m_z$  is finite. The direction of  $\mathbf{k}_i$  is depicted in the inset panels and we understand that  $I_{\pi-\sigma'}$  becomes nearly zero in Fig. 2h because – assuming a spin helix – the relative angle between  $\mathbf{k}_i$  and  $\mathbf{m}_{\text{ip}}$  approaches  $90^\circ$ . In summary, we identify the magnetic ground state as a coplanar spin helix, characterized by the commensurate propagation vector  $\mathbf{k}_{\text{mag}} = (1/6, 1/6, 0)$ , as depicted in Fig. 2i and discussed further in Supplementary Information. This magnetic structure breaks space inversion symmetry but preserves the combined spin rotation and translation operation  $[C_{2\perp} \parallel \mathbf{t}_{1/2}]$  as well as  $[\mathcal{T} \parallel \mathbf{t}_{1/2}]$ , consistent with  $p$ -wave magnetism.

### Electronic anisotropy of a $p$ -wave magnet

Electronic transport measurements on mesoscopic devices are suitable to detect the predicted electronic anisotropy of the  $p$ -wave state, where the directions parallel and perpendicular to the spin polarization vector  $\boldsymbol{\alpha}$  are not equiva-

lent [12–14]. To suppress extrinsic pinning of  $\alpha$  due to anisotropic strain, we used the focused ion beam technique to cut a free-standing, circular device with meandering contacts as strain relief (Fig. 3a, Methods). We use this device to simultaneously probe the resistance of current flow along three symmetry-equivalent directions of the hexagonal crystal structure, which become inequivalent when the magnetic state is formed (Fig. 3b). We warm the device from base temperature and observe its resistivity in Fig. 3c; the device shows magnetic phase transitions in good agreement with the bulk magnetization (red trace).

Applying a finite magnetic field perpendicular to the  $c$ -axis and rotating the sample by the angle  $\phi$ , we observe a characteristic two-fold anisotropic resistivity in Fig. 3d-f below the magnetic transition – as compared to a weak, conventional anisotropic resistivity [24] in the paramagnetic state (Fig. 3d, white circles). For each magnetic field direction, one of the three current directions  $I_a$ ,  $I_b$ , or  $I_c$  has a large resistance, and the other two have low resistance. This demonstrates the selection of a dominant domain of  $\mathbf{k}_{\text{mag}}$  by the magnetic field. Following the conventions of Fig. 1a, the insets in Fig. 3d show the evolution of  $\alpha$  in discrete steps during the field rotation, and confirm that it is easier for the current to flow along the direction perpendicular to  $\alpha$ .

### Zero-field, giant anomalous Hall effect induced by time reversal breaking

We now set the magnetic field  $B$  along the crystallographic  $c$ -axis and find that, in Fig. 4a, the magnetization increases roughly linearly and approaches the saturation value  $M_{\text{sat}}$  expected for  $\text{Gd}^{3+}$  moments (Methods). Around zero magnetic field, there appears a tiny spontaneous magnetization  $m_z$  of about 2% of  $M_{\text{sat}}$  with a coercive field of about 0.15 T. Such a tiny parasitic  $m_z$  corresponds to a  $\mathcal{T}$ -breaking distortion of the  $p$ -wave state, which has been predicted in models of itinerant electrons coupled to localized magnetic moments [15].

A surprising transport response appears when  $B$  is parallel to the  $c$ -axis: a sharp, giant anomaly of the Hall effect around  $B = 0$ , which is smoothly suppressed when moving into the regime of higher magnetic fields. When the magnetization is close to saturation, the Hall effect returns to conventional behaviour, being composed of a magnetization-dependent term and a term linear in  $B$ :  $\sigma_{xy} = S_0 B + S_A \mu_0 M$  with constants  $S_0$  and  $S_A$  (Methods) [25]. The strongly  $B$ -dependent contribution  $\Delta\sigma_{xy}$  in the  $p$ -wave state is isolated by subtracting these two terms, and the resulting traces of  $\Delta\sigma_{xy}$  are shown in Fig. 4c,d. We note that  $\Delta\sigma_{xy}$  appears at near-zero net magnetization as a zero-field, anomalous Hall effect (AHE).

Figure 4e summarizes the zero-field AHE in various bulk antiferromagnets, providing perspective for the large response realized in the present candidate  $p$ -wave magnet. In particular, our material has a Hall conductivity in excess of 600 S/cm, comparable to the intrinsic anomalous Hall effect of a ferromagnet. In contrast to other antiferromagnets with a large AHE and small net magnetization,  $M(H)$  approaches saturation at a modest and easily accessible magnetic field [26–31]. It is thus possible to switch between the antiferromagnetic  $p$ -wave and ferromagnetic states within a reasonable window of experimental parameters.

### Anomalous Hall effect from lifted nodal plane degeneracies

The simplest low-energy model that respects the symmetries of a  $p$ -wave magnet –  $[C_{2\perp} \parallel \mathbf{t}_{1/2}]$  and  $[\mathcal{T} \parallel \mathbf{t}_{1/2}]$  – and which motivates the observed AHE is a  $2 \times 2$  matrix taking into account the spin-polarized band states, weak spin-orbit coupling (SOC), and the small net magnetization  $m_z$  (Methods)

$$\mathcal{H}(\mathbf{k}) = \mathbf{k}^2 \sigma_0 + p k_x \sigma_x + m_z \sigma_z + \lambda k_y \sigma_y = \mathbf{k}^2 \sigma_0 + \sum_i d_i \sigma_i, \quad (1)$$

where  $\sigma_0$  is the identity matrix and  $\sigma_x$ ,  $\sigma_y$ ,  $\sigma_z$  are Pauli matrices. The Berry curvature  $\Omega_{xy}^\pm = \mp \epsilon_{abc} d_a \partial_{k_x} d_b \partial_{k_y} d_c / (2|\mathbf{d}|^3)$  of the upper (+) and lower (–) band is conveniently expressed through the components  $d_i$  of a vector  $\mathbf{d}$ , where  $\epsilon_{abc}$  is the Levi-Civita symbol. This expression implies that all three components of the  $\mathbf{d}$ -vector should be finite for non-zero  $\Omega_{xy}^\pm$ .

As shown in Fig. 1c, this model produces a spin-dependent band splitting along  $k_x$ , where the two bands are degenerate on the  $k_x = 0$  plane when  $m_z = 0$ . The symmetry-protected spin-nodal plane is clearly seen in Fig. 1e as a plane where the spin polarization switches its sign. Adding  $m_z$  and spin-orbit coupling (SOC), we observe strongly enhanced Berry curvature  $\Omega_{xy}$  close to the spin-nodal plane (Fig. 1f). The large *susceptibility* of  $\sigma_{xy}$  to  $m_z$  has its origin in the symmetry-protected nodal planes of the undistorted ( $m_z = 0$ )  $p$ -wave state.

### Conclusions

The present spin helix in direct space satisfies the symmetry requirement of combined time reversal and translation symmetry  $[C_{2\perp} \parallel \mathbf{t}_{1/2}]$ , up to a tiny net magnetization  $m_z$ . We have demonstrated the anisotropic electronic properties of this candidate  $p$ -wave state, and revealed a surprisingly large anomalous Hall effect in zero magnetic field, which requires spin-orbit coupling and  $m_z$ . Recent theoretical studies predict the generation of large linear and non-linear spin currents in  $p$ -wave magnets, as well as a large tunneling magnetoresistance and unconventional

superconducting proximity effects [6, 14, 17, 32–34]. In particular, it is believed that the low number of nodal planes in spin-split  $p$ -wave antiferromagnets is advantageous for functionality as a spin injector [32, 33]. Therefore,  $p$ -wave magnets may serve as an ideal platform to explore the interplay of unconventional magnetism, spintronics, electronic band topology, and superconductivity.

- 
- [1] K.-H. Ahn, A. Hariki, K.-W. Lee, and J. Kuneš, Phys. Rev. B **99**, 184432 (2019).
  - [2] M. Naka, S. Hayami, H. Kusunose, Y. Yanagi, Y. Motome, and H. Seo, Nat. Commun. **10**, 4305 (2019).
  - [3] L. Šmejkal, R. González-Hernández, T. Jungwirth, and J. Sinova, Sci. Adv. **6**, eaaz8809 (2020).
  - [4] L. Šmejkal, J. Sinova, and T. Jungwirth, Phys. Rev. X **12**, 040501 (2022).
  - [5] L. Šmejkal, J. Sinova, and T. Jungwirth, Phys. Rev. X **12**, 031042 (2022).
  - [6] M. Ezawa, arXiv:2411.16036 (2024).
  - [7] J. E. Hirsch, Phys. Rev. B **41**, 6820 (1990).
  - [8] C. Wu, K. Sun, E. Fradkin, and S.-C. Zhang, Phys. Rev. B **75**, 115103 (2007).
  - [9] J. Jung, M. Polini, and A. H. MacDonald, Phys. Rev. B **91**, 155423 (2015).
  - [10] E. I. Kiselev, M. S. Scheurer, P. Wölfle, and J. Schmalian, Phys. Rev. B **95**, 125122 (2017).
  - [11] Y.-M. Wu, A. Klein, and A. V. Chubukov, Phys. Rev. B **97**, 165101 (2018).
  - [12] A. B. Hellenes, T. Jungwirth, A. C. Rodrigo Jaeschke-Ubiergo, J. Sinova, and L. Šmejkal, arXiv preprint arXiv:2309.01607 (2023).
  - [13] T. Jungwirth, R. M. Fernandes, E. Fradkin, A. H. MacDonald, J. Sinova, and L. Smejkal, arXiv:2411.00717 (2024).
  - [14] M. Ezawa, arXiv:2410.21854 (2024).
  - [15] S. Okumura, Y. Kato, and Y. Motome, J. Phys. Soc. Jpn. **87**, 033708 (2018).
  - [16] B. Brekke, P. Sukhachov, H. G. Giil, A. Brataas, and J. Linder, Phys. Rev. Lett. **133**, 236703 (2024).
  - [17] M. Ezawa, Phys. Rev. B **110**, 165429 (2024).
  - [18] R. E. Gladyshevskii, O. R. Strusievicz, K. Cenozal, and E. Parthé, Acta Crystallogr. B **49**, 474 (1993).
  - [19] J. Niermann and W. Jeitschko, Z. Anorg. Allg. Chem. **628**, 2549 (2002).
  - [20] M. A. Ruderman and C. Kittel, Phys. Rev. **96**, 99 (1954).
  - [21] T. Kasuya, Prog. Theor. Phys. **16**, 45 (1956).
  - [22] K. Yosida, Phys. Rev. **106**, 893 (1957).
  - [23] S. W. Lovesey and S. P. Collins, *X-ray scattering and absorption by magnetic materials*, no. 1 in Oxford series on synchrotron radiation (Clarendon Press, Oxford University Press, 1996).
  - [24] T. McGuire and R. Potter, IEEE Transactions on Magnetism **11**, 1018 (1975).
  - [25] N. Nagaosa, J. Sinova, S. Onoda, A. H. MacDonald, and N. P. Ong, Rev. Mod. Phys. **82**, 1539 (2010).
  - [26] S. Nakatsuji, N. Kiyohara, and T. Higo, Nature **527**, 212 (2015).
  - [27] A. K. Nayak, J. E. Fischer, Y. Sun, B. Yan, J. Karel, A. C. Komarek, C. Shekhar, N. Kumar, W. Schnelle, J. Kübler, et al., Sci. Adv. **2**, e1501870 (2016).
  - [28] N. J. Ghimire, A. S. Botana, J. S. Jiang, J. Zhang, Y.-S. Chen, and J. F. Mitchell, Nat. Commun. **9**, 3280 (2018).
  - [29] H. Takagi, R. Takagi, S. Minami, T. Nomoto, K. Ohishi, M.-T. Suzuki, Y. Yanagi, M. Hirayama, N. D. Khanh, K. Karube, et al., Nat. Phys. **19**, 961 (2023).
  - [30] P. Park, W. Cho, C. Kim, Y. An, Y.-G. Kang, M. Avdeev, R. Sibille, K. Iida, R. Kajimoto, K. H. Lee, et al., Nat. Commun. **14**, 8346 (2023).
  - [31] L. Šmejkal, A. H. MacDonald, J. Sinova, S. Nakatsuji, and T. Jungwirth, Nat. Rev. Mater. **7**, 482 (2022).
  - [32] B. Brekke, P. Sukhachov, H. G. Giil, A. Brataas, and J. Linder, arXiv preprint arXiv:2405.15823 (2024).
  - [33] A. A. Hedayati and M. Salehi, arXiv preprint arXiv:2408.10413 (2024).
  - [34] K. Maeda, B. Lu, K. Yada, and Y. Tanaka, J. Phys. Soc. Jpn. **93**, 114703 (2024).
  - [35] A. Aharoni, J. Appl. Phys. **83**, 3432 (1998), ISSN 0021-8979.

## Methods

**Crystal growth and characterization.** Single crystals of  $\text{Gd}_3(\text{Ru}_{1-x}\text{Rh}_x)_4\text{Al}_{12}$  were synthesized under Ar gas flow in a high-vacuum floating zone (FZ) furnace. The sample quality is confirmed by powder X-ray diffraction (XRD), energy-dispersive X-ray spectroscopy (EDX), and by examination under an optical polarization microscope. We used Laue XRD and a diamond saw to precisely orient and align the sample surfaces.

**Magnetization and electrical transport measurements on bulk samples.** Magnetization was measured in a commercial Quantum Design MPMS3 (DC-mode) and Quantum Design PPMS-14T (VSM, vibrating sample magnetometer). The magnetic field is applied along the crystallographic  $c$ -axis of the crystal. Electrical transport measurements were performed on polished single crystal plates with electrical contacts made of  $30\ \mu\text{m}$  gold wires, using silver paste (Dupont). We set the sample surface perpendicular to the  $c$ -axis ( $\mathbf{B} \parallel \mathbf{c}$ ) and applied the electric current along the  $a$ -axis to measure the data in Fig. 4. We perform a demagnetization correction by assuming that the sample shape is an ellipsis to compare field-dependent physical properties of samples with different shapes [35].

**Focused ion beam device fabrication and measurements.** Using a Thermo Fischer Helios 5UX focused ion beam (FIB) system, a lamella of  $\text{Gd}_3(\text{Ru}_{0.95}\text{Rh}_{0.05})_4\text{Al}_{12}$  was carved and extracted from the bulk crystal, thinned down, and shaped into a circle. Using an in-situ micro-manipulator, this circle was placed on to a  $\text{Al}_2\text{O}_3$  substrate patterned with Au contacts, and attached with ion-beam induced Pt deposition. The meander-shaped bonds and final sample geometry were created with a final ion milling step. The entire device was coated in a capping layer of  $5\ \text{nm}$  of  $\text{Al}_2\text{O}_3$  using atomic layer deposition. The anisotropic resistance of the finished device was measured in a Quantum Design PPMS-14T as described in the previous Methods paragraph, using the as-provided rotator probe option.

**Resonant elastic X-ray scattering (REXS).** Magnetic resonant elastic X-ray scattering (REXS) experiments were conducted at BL-3A (KEK, Photon Factory, Japan) using the Gd- $L_2$  absorption edge. The scattering plane is  $(H, K, 0)$ , so that the incoming and outgoing beam wave vectors  $\mathbf{k}_i$  and  $\mathbf{k}_f$  are perpendicular to the crystallographic  $c$ -axis. We used the (006) reflection of a pyrolytic graphite plate ( $2\theta \sim 88^\circ$  at the Gd- $L_2$  edge) to perform the polarization analysis of the scattered X-ray beam (see Fig. 2c and Supplementary Information for more details). We define the orientation of the detector with respect to the scattering plane by an angle  $\gamma$  such that  $\gamma = 0^\circ$  detects the  $\pi - \sigma'$  component of the scattered X-ray beam, whereas the  $\pi - \pi'$  component is detected in the out-of-plane orientation of the detector at  $\gamma = 90^\circ$ .

**Collinear spin expectation value in momentum space.** In magnetic structures with  $[C_{2\perp} \parallel \mathbf{t}_{1/2}]$  and  $[\mathcal{T} \parallel \mathbf{t}_{1/2}]$  symmetries, as well as sufficiently small spin-orbit coupling (SOC), there exists a good spin quantum number in momentum space. This means all bands and eigenstates can be labelled using spin symmetry eigenvalues  $\lambda_s$ . We introduce the composite operator  $U_s \mathbf{t}_{1/6}$  with the intention of defining the  $\lambda_s$ : a sixfold spin-rotation around the  $x$ -axis,  $U_s = \exp(i\frac{2\pi}{6} \frac{s_x}{\hbar})$ , combined with a translation  $\mathbf{t}_{1/6} = \mathbf{a}_o/6 + \mathbf{b}_o/2$ . Here,  $s_x$  is the spin-1/2 operator component. We use the lattice vectors  $\mathbf{a}_o$ , and  $\mathbf{b}_o$  of the folded magnetic unit cell (orthorhombic), with lattice constants  $a_o$ ,  $b_o$  – as in Fig. 2d.

Let a Hamiltonian of conduction electrons be exchange-coupled to the magnetic state discussed in the main text. Without SOC, this Hamiltonian commutes with  $U_s \mathbf{t}_{1/6}$ ; the two operators share a common eigenbasis. The third power of  $U_s \mathbf{t}_{1/6}$  is  $\sim s_x \mathbf{t}_{1/2}$ , so that the eigenstates of the former are also eigenstates of the latter – however, they are not eigenstates of the operator  $s_x$  itself. We choose the  $\lambda_s$  as the two eigenvalues of  $(U_s \mathbf{t}_{1/6})^3$ . Thus, there is a spin symmetry with two eigenvalues  $\lambda_s$  that commutes with the Hamiltonian and that labels band pairs at every momentum  $\mathbf{k}$ . In the limit of the low energy model, the translation part of the symmetries is lost and the  $\lambda_s$  reduce to spin expectation values  $\langle s_x \rangle$ .

**Low-energy model from symmetries.** Starting from the point-group symmetries of  $p$ -wave magnets, we construct a low-energy model describing an electronic band in two dimensions, coupled to the magnetic texture. In the limit of long wavelengths, around  $\mathbf{k} = 0$ , the symmetries  $[C_{2\perp} \parallel \mathbf{t}_{1/2}]$  and  $[\mathcal{T} \parallel \mathbf{t}_{1/2}]$  reduce to the point group operations  $C_{2\perp} = i\sigma_x$  and  $\mathcal{T} = i\sigma_y K$  with the complex conjugation  $K$ . Without SOC, the Hamiltonian is required to commute with  $C_{2\perp}$ , and further, is required to be consistent with  $p$ -wave time-reversal symmetry  $\mathcal{T}^{-1}H(\mathbf{k})\mathcal{T} = H(-\mathbf{k})$ . To linear order, all allowed terms are equivalent to  $pk_x\sigma_x$ . As for spin-orbit coupling (SOC), we consider leading-order terms that are allowed due to broken inversion symmetry in the  $p$ -wave state. The spin rotation  $C_{2\perp}$  can now be broken and any term of the form  $k_i\sigma_j$  with  $i \in \{x, y\}$  and  $j \in \{x, y, z\}$  is consistent with  $\mathcal{T}$ . However, SOC does not break a combined rotation  $C_{2x}$  in spin and direct spaces, which is characteristic for the magnetic state depicted in Fig. 2i. We focus on the simplest term consistent with  $C_{2x}$ ,  $\lambda k_y\sigma_y$ . Finally, the kinetic energy of a

parabolic band is  $k^2\sigma_0$  and the Zeeman energy for a magnetic field  $\mathbf{B} \parallel z$  is  $B\sigma_z$ . These considerations lead to Eq. (1).

**Spin-nodal plane in momentum space.** In the following, we make some more general remarks on the electronic structure of the  $p$ -wave magnet. We can argue for the existence of degenerate nodal planes in momentum space by invoking  $[\mathcal{T} \parallel \mathbf{t}_{1/2}]$  symmetry on the eigenstates of  $(U_s \mathbf{t}_{1/6})^3$  with eigenvalues  $\pm\lambda_s$ . The  $\mathcal{T}$  operation comprises complex conjugation of wavefunctions and a spin flip, so we have  $\mathcal{T}U_s = -U_s\mathcal{T}$ . This yields  $E(\mathbf{k}) = E(-\mathbf{k})$ , since two eigenstates of the Hamiltonian are related by  $\mathcal{T}|E, \mathbf{k}, \lambda_s\rangle \propto |E, -\mathbf{k}, -\lambda_s\rangle$ . We showed above that  $\lambda_s$  is a good quantum number for all crystal momenta  $\mathbf{k}$ ; hence, along any line connecting the momenta  $\mathbf{k}$  and  $-\mathbf{k}$ , there must be an odd number of exchanges between eigenstates labelled by  $+\lambda_s$  and  $-\lambda_s$ . This implies an odd number of nodal planes on which the energy bands of the Hamiltonian are two-fold degenerate in absence of SOC.

**Pinning of nodal plane to high symmetry directions.** We discuss symmetry constraints that force the nodal planes to be flat and spanned by high-symmetry directions in  $\mathbf{k}$ -space. Again invoking the  $C_{2x}$  symmetry and combining with  $\mathcal{T}$ , we define  $\mathcal{G} = C_{2x}\mathcal{T}$ . This  $\mathcal{G}$  commutes with the Hamiltonian and anti-commutes with  $(U_s \mathbf{t}_{1/2})^3$  up to a full lattice translation. In addition,  $\mathcal{G}$  acts on crystal momenta like a mirror operation,  $(k_x, k_y, k_z) \rightarrow (-k_x, k_y, k_z)$ . Thus,  $\mathcal{G}$  enforces a nodal plane at  $k_x = 0$ , where the eigenvalues  $\pm\lambda_s$  label states of degenerate energy.

### Acknowledgments

We acknowledge Akiko Kikkawa for help in crystal growth. We also acknowledge support from the Japan Society for the Promotion of Science (JSPS) under Grant Nos. JP22H04463, JP23H05431, JP22F22742, JP22K20348, JP23K13057, JP24H01607, and JP24H01604, as well as from the Murata Science Foundation, Yamada Science Foundation, Hattori Hokokai Foundation, Mazda Foundation, Casio Science Promotion Foundation, Inamori Foundation, and Kenjiro Takayanagi Foundation. This work was partially supported by the Japan Science and Technology Agency via JST CREST Grant Numbers JPMJCR1874, JPMJCR20T1 (Japan) and JST FOREST (JPMJFR2238). It was also supported by Japan Science and Technology Agency (JST) as part of Adopting Sustainable Partnerships for Innovative Research Ecosystem (ASPIRE), Grant Number JPMJAP2426. P.R.B. acknowledges Swiss National Science Foundation (SNSF) Postdoc.Mobility grant P500PT\_217697 for financial assistance. Mo. H. is funded by the Deutsche Forschungsgemeinschaft (DFG, German Research Foundation) - project number 518238332. Resonant X-ray scattering at Photon Factory (KEK) was carried out under proposal numbers 2022G551 and 2023G611. The neutron experiment at the Materials and Life Science Experimental Facility of J-PARC was performed under a user program (Proposal No. 2020B0347).

### Author contributions

Ma.H., Y.Mo., T.A., and Y.To. conceived the project. R.Y. and Ma.H. grew and characterized the single crystals. R.Y., R.N., and Ma.H. performed magnetization and transport measurements on bulk samples. M.B. prepared focused ion beam devices and performed all device measurements. H.S., H.N., and Ma.H. performed resonant X-ray scattering experiments and analyzed data with P.R.B. S.G., K.O., K.K., and Ma.H. performed neutron scattering experiments, while the data was analyzed by P.R.B. and Y.I. S.O., Mo.H., and Y.Mo. performed symmetry analysis and low-energy model calculations. R.Y., M.B., P.R.B., and Ma.H. wrote the manuscript; all authors discussed the results and commented on the manuscript.

## Main Text Figures

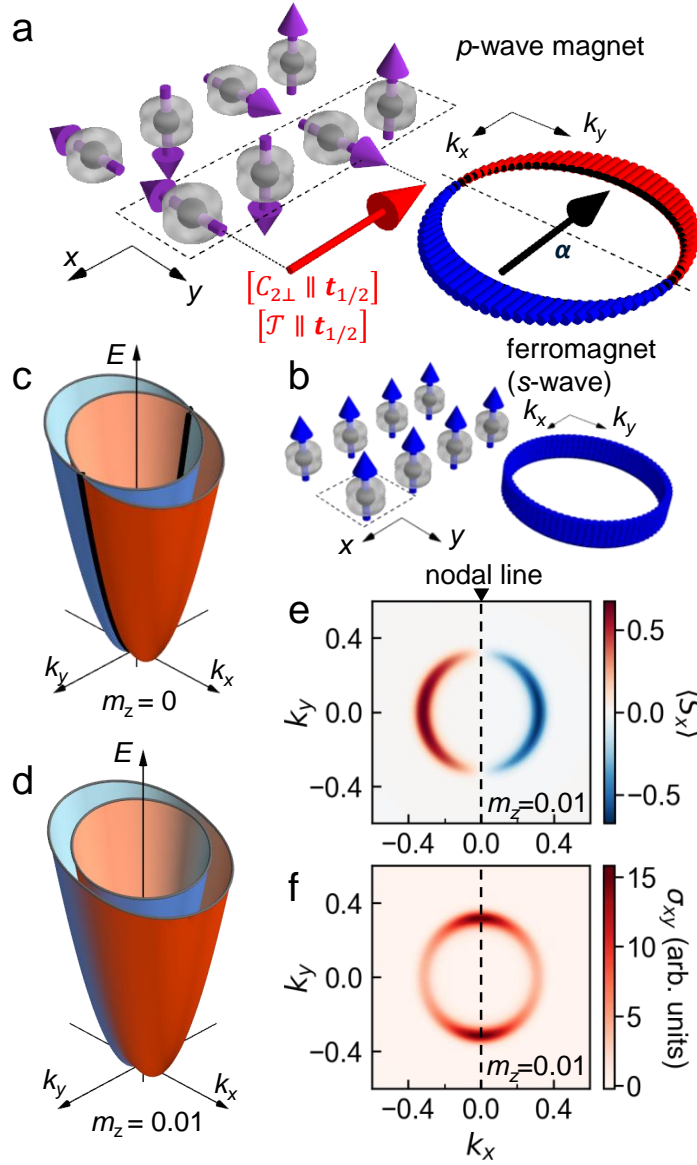


FIG. 1: **Magnetic structure of a  $p$ -wave magnet in direct space and spin-split electronic bands in momentum space.** **a**, Non-collinear spin modulation in direct space and alternating spin polarization in momentum ( $\mathbf{k}$ -)space. Red and blue bars: momentum-resolved expectation value of  $S_x(\mathbf{k})$  at the chemical potential. For commensurate order with wavelength  $\lambda = N$  (even integer  $N$ ), this state is unchanged under  $180^\circ$  spin rotation followed by translation of half a lattice constant, termed  $[C_{2\perp} \parallel \mathbf{t}_{1/2}]$  symmetry. The spin polarization vector in momentum space is  $\alpha$  [14]. **b**, Ferromagnets have spins along the  $z$ -axis in direct space and a uniform spin polarization  $S_z(\mathbf{k})$  in  $\mathbf{k}$ -space (right). **c**, Minimal electronic structure model for a  $p$ -wave magnet. The spin-splitting of bands causes two-fold electronic anisotropy. Red (blue) indicate spin parallel (antiparallel) to  $k_x$ . **d**, Electronic structure in presence of a tiny net magnetization  $m_z$ . **e**, Spin polarization  $S_x$  when  $m_z \neq 0$ . **f**, Anomalous Hall conductivity  $\sigma_{xy}$  induced by Berry curvature appears in the  $k_x$ - $k_y$  plane when  $m_z \neq 0$ , due to lifting the band degeneracy of the nodal plane.

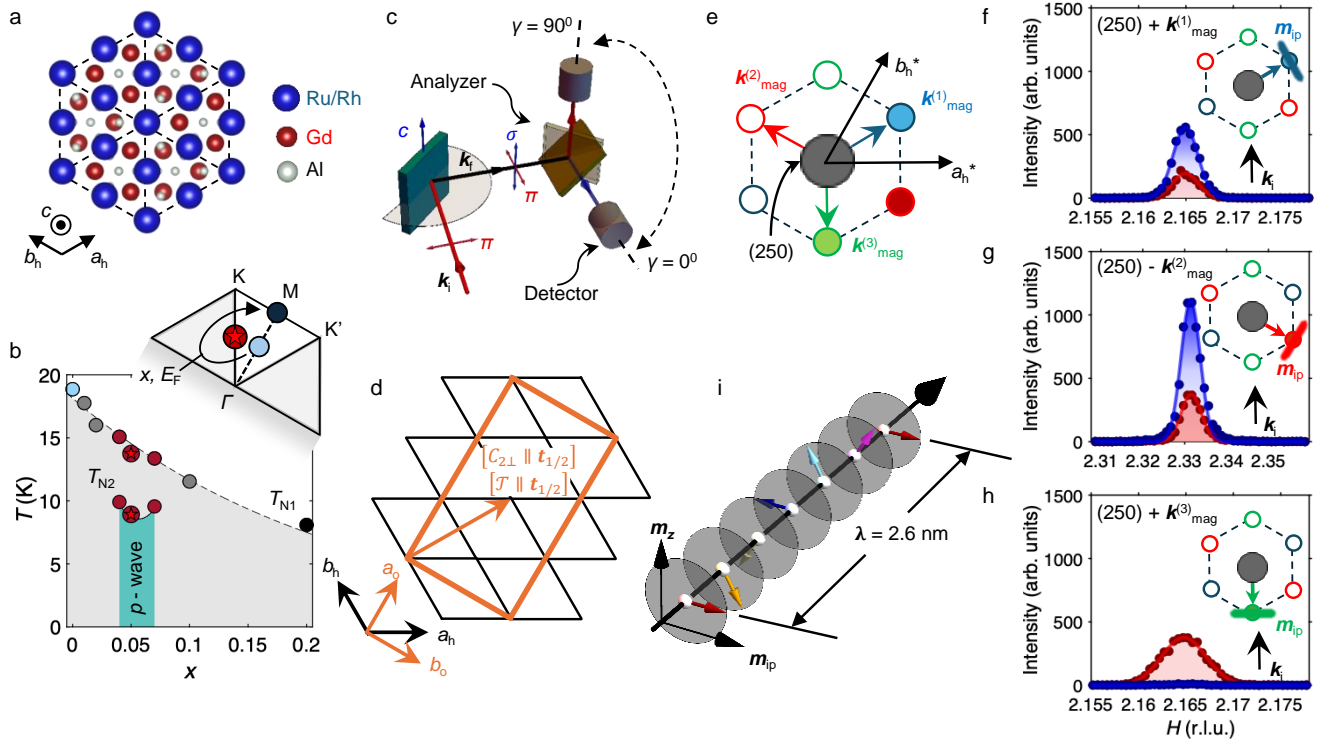
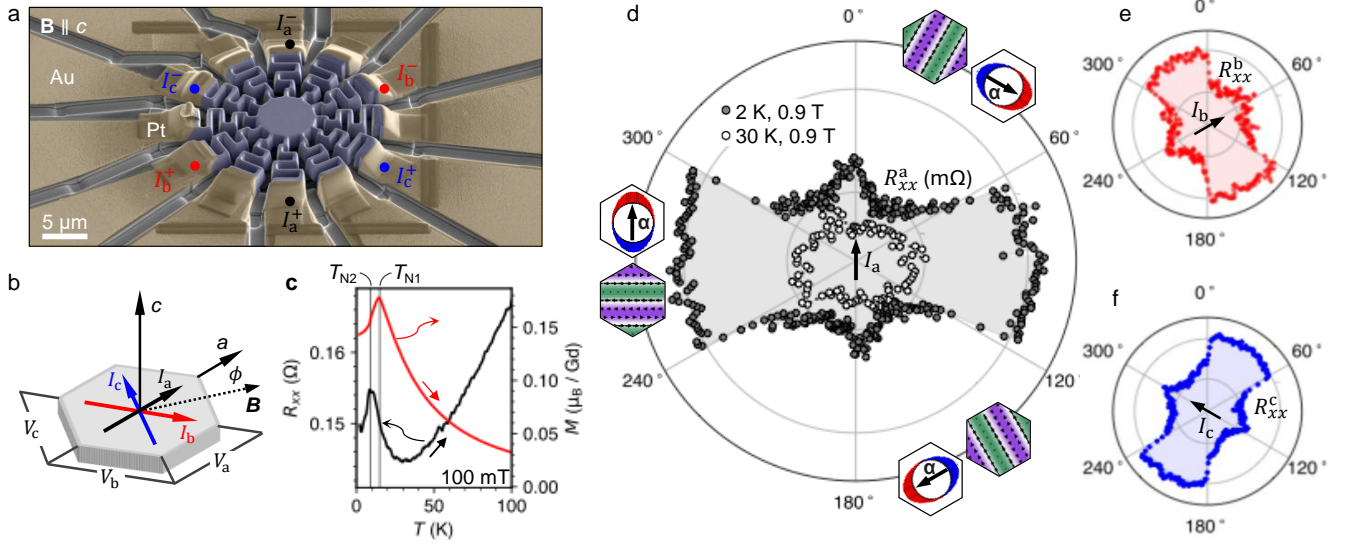


FIG. 2: **Commensurate spin helix in direct space, consistent with  $p$ -wave magnetism, revealed by resonant elastic X-ray scattering (REXS).** **a**, Crystal structure of hexagonal  $\text{Gd}_3(\text{Ru}_{1-x}\text{Rh}_x)_4\text{Al}_{12}$ . **b**, Tuning the magnetic propagation vector  $\mathbf{k}_{\text{mag}}$  by chemical substitution of Rh for Ru. Inset: Evolution of the magnetic ordering vector  $\mathbf{k}_{\text{mag}}$  with  $x$ :  $\mathbf{k}_{\text{mag}} = (1/6, 1/6, 0)$  appears for  $x = 0.04 - 0.07$ , c.f. shaded region in main panel. For  $x = 0$  and  $x = 0.2$  the magnetic wavevectors are  $(0.272, 0, 0)$  and  $(0.5, 0, 0)$ , respectively. Momenta are expressed in reciprocal lattice units (r.l.u.) and only half of the first hexagonal Brillouin zone is shown, sliced at  $k_z = 0$ . **c**, Single crystal REXS experiments in reflection geometry, with incoming and outgoing beams  $\mathbf{k}_i$ ,  $\mathbf{k}_f$  spanning the scattering plane (light grey). In polarization analysis,  $I_{\pi-\pi'}$  and  $I_{\pi-\sigma'}$  components of  $\mathbf{k}_f$  are separated by rotating the detector around an analyzer plate by the angle  $\gamma$  (Methods). **d**, Crystallographic unit cells (hexagonal, black grid) and reconstructed magnetic unit cell (orthorhombic, orange box). The requirements for  $p$ -wave magnetism,  $[C_{2\perp} \parallel \mathbf{t}_{1/2}]$  and  $[\mathcal{T} \parallel \mathbf{t}_{1/2}]$  symmetry, are satisfied by the orange arrow. **e**, Due to the formation of three  $p$ -wave magnetic domains, six magnetic reflections appear in a given Brillouin zone. **f-h**, Polarization analysis using magnetic satellites around the fundamental  $(2, 5, 0)$  reflection. Insets: Geometry of  $\mathbf{k}_i$  relative to the modulated magnetization projected into the scattering plane,  $\mathbf{m}_{\text{ip}}$ . **i**, Illustration: Commensurate spin helix with short wavelength  $\lambda$  in direct space.





**FIG. 3: Anisotropic electronic transport properties.** **a**, Scanning electron micrograph of the rotationally symmetric focused ion beam device. The meander-shaped arms release the strain on the device, which arises due to thermal expansion mismatch of device and substrate. The false colour regions indicate the target material (blue) and the electrical contacts (orange), which are composed of evaporated gold (Au) wires and ion beam-deposited platinum (Pt), respectively. The contacts utilised in the directional transport measurements are labelled and colour coded. The scale bar is  $5\ \mu\text{m}$ . **b**, Device geometry with crystal axes  $a$ ,  $c$  and three pairs of current contacts  $I_a$ ,  $I_b$ ,  $I_c$ ; the corresponding longitudinal voltage drops  $V_a$ ,  $V_b$ ,  $V_c$  are measured simultaneously. The magnetic field  $\mathbf{B}$  is rotated by an angle  $\phi$  to the  $a$ -axis. **c**, Temperature-dependent traces of longitudinal resistance (left) and magnetization  $M$  (right), with two antiferromagnetic transitions  $T_{N1}$  and  $T_{N2}$ . **d**, Change in longitudinal resistance when switching between different  $p$ -wave domains by a small magnetic field of  $0.9\ \text{T}$ ; the insets illustrate the deduced direction of the spin polarization vector  $\alpha$  in momentum space, and the periodic spin texture in direct space, for each sextant of the magnetic field angle. Two-fold anisotropy emerges, with higher resistance for current  $I_a$  (center arrow) parallel to  $\alpha$ . Open circles: Data at  $30\ \text{K} > T_{N1}$  plotted for comparison. **e, f** Simultaneous measurements for other contact pairs, demonstrating the anisotropic resistance is due to the relative alignment between current and  $\alpha$ .

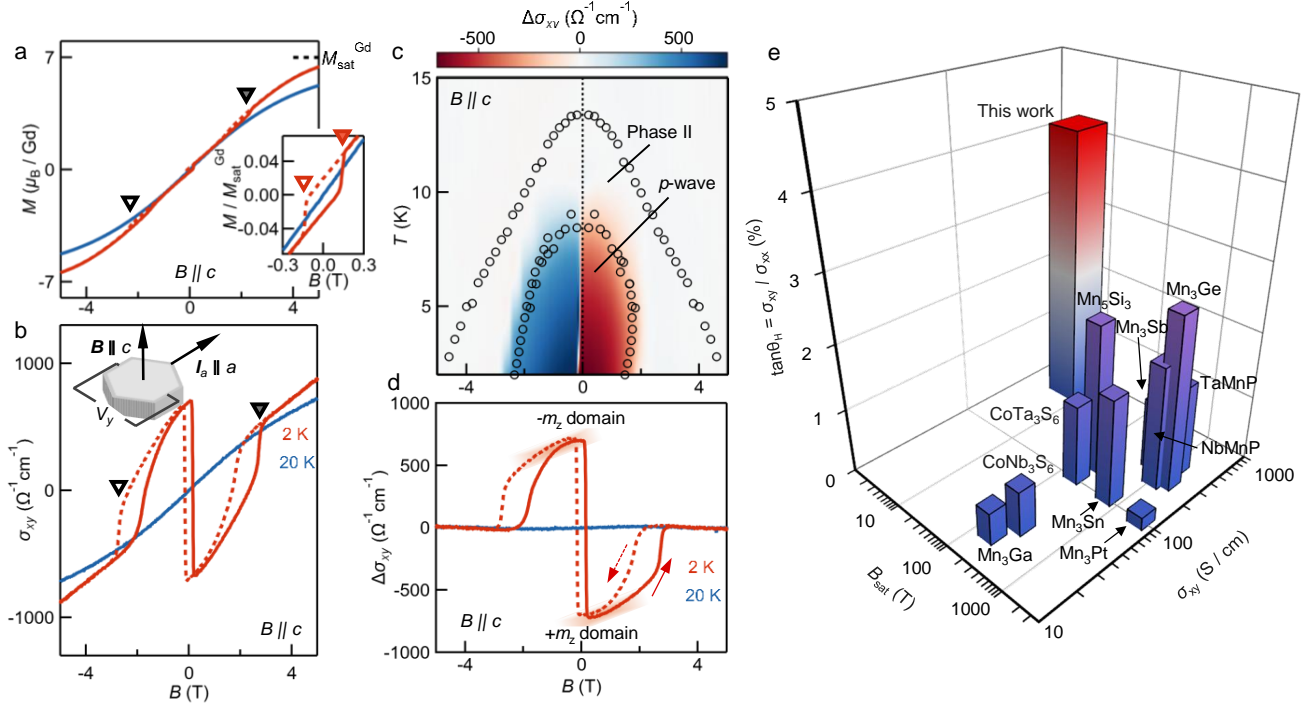


FIG. 4: **Giant anomalous Hall effect (AHE) induced by a tiny net magnetization  $m_z$  and spin-orbit coupling (SOC).** **a**, Comparison of net magnetization  $M(B)$  measured at  $T = 2$  K and 20 K. The magnetic field is applied along the  $c$ -axis. Inset: small spontaneous magnetization  $m_z$  appears around zero field below  $T_{N2}$ . **b**, Hall conductivity with large zero-field (anomalous) value  $\sigma_{xy}^A$  reaching up to  $600 \Omega^{-1} \text{cm}^{-1}$ . **c,d**, Hall conductivity  $\Delta\sigma_{xy}$  after subtraction of components proportional to the magnetic field and to the magnetization.  $\Delta\sigma_{xy}$  is enhanced in the  $p$ -wave magnetic phase I. Open circles marking the phase boundaries in panel **c** are obtained from magnetization measurements in Supplementary Information. **e**, As compared to other bulk antiferromagnets with AHE, our distorted  $p$ -wave state in  $\text{Gd}_3\text{Ru}_4\text{Al}_{12}$  has large  $\sigma_{xy}^A$  induced by  $m_z$ , large Hall angle  $\sigma_{xy}^A/\sigma_{xx}$ , and a low saturation magnetic field  $B_{\text{sat}}$ . Raw data for the bar plot are provided in Supplementary Information.